Annals of Nuclear Medicine
https://doi.org/10.1007/s12149-021-01669-6

ORIGINAL ARTICLE

Development of radioiodinated pyrimidinopyridone derivatives as targeted imaging probes of activated p38α for single photon emission computed tomography

Tomoyuki Hashimoto[1] · Naoya Kondo[1] · Masahiko Hirata[1] · Takashi Temma[1]

Received: 11 May 2021 / Accepted: 9 August 2021

Abstract

Objective p38α, a member of the mitogen-activated protein kinase superfamily, is ubiquitously expressed in a variety of mammalian cells. Activated p38α induces inflammatory responses to external stimuli, suggesting that non-invasive detection of activated p38α would be valuable for diagnosing inflammatory diseases. For this purpose, we designed radiolabeled compounds [^{123}I]2-IR and [^{123}I]4-IR based on a potent p38α selective inhibitor R1487 for use with single photon emission computed tomography (SPECT). In this study, we used ^{125}I instead of ^{123}I due to its more usable radiochemical properties, synthesized [^{125}I]2-IR and [^{125}I]4-IR, and evaluated their effectiveness as activated p38α imaging probes.

Methods [^{123}I]2-IR and [^{123}I]4-IR were designed by introduction of a ^{123}I atom at the 2- or 4-ositions of the phenoxy ring, preserving the pyrimidinopyridone structure of R1487. We synthesized 2-IR and 4-IR via a 7-step process. The inhibitory potencies of 2-IR, 4-IR, and p38α inhibitors were measured using an ADP-Glo™ kinase assay system. Radioiodination of 2-IR and 4-IR was performed via an organotin-radioiodine exchange reaction using the corresponding tributyltin precursors. Biodistributions were evaluated by determining radioactivity in tissues of interest after intravenous administration of [^{125}I]2-IR and [^{125}I]4-IR in normal ddY mice and turpentine oil-induced inflammation model mice. In vivo inhibition study was also performed in inflammation model mice after intravenous administration of [^{125}I]4-IR with pretreatment of p38α inhibitors.

Results We synthesized 2-IR and 4-IR at total yields of 17.5% and 19.2%, respectively. 4-IR had higher p38α inhibitory potency than 2-IR; both compounds were significantly less potent than R1487. [^{125}I]2-IR and [^{125}I]4-IR were successfully obtained from tributyltin precursors with high radiochemical yield (> 65%), purity (> 97%), and molar activity (~ 81 GBq/μmol). [^{125}I]4-IR showed high radioactivity accumulation in the inflamed tissue (7.0 ± 1.2%D/g), rapid delivery throughout the body, and rapid blood clearance, resulting in a high inflammation-to-blood ratio (6.2 ± 0.4) and a high inflammation-to-muscle ratio (5.2 ± 1.3) at 30 min, while [^{125}I]2-IR showed low radioactivity accumulation in inflamed tissue over the experimental period. Further, radioactivity accumulation in inflamed tissue after [^{125}I]4-IR administration was significantly decreased by pretreatment with selective inhibitors.

Conclusions [^{123}I]4-IR would be a promising imaging agent for detection of activated p38α.

Keywords p38α · Inflammation · Single photon emission computed tomography · Pyrimidinopyridone radioiodine

Introduction

p38 is a Ser/Thr kinase that is a mitogen-activated protein kinase (MAPK) and a member of the MAPK superfamily. Several MAPK signaling cascades are activated in response to environmental stresses such as osmotic shock and infection [1, 2] and are also important regulators of the biosynthesis of inflammatory cytokines at transcriptional and translational levels. Among the four subtypes, p38α is ubiquitously expressed in a variety of mammalian cells [3] and

✉ Takashi Temma
takashi.temma@ompu.ac.jp

[1] Department of Biofunctional Analysis, Graduate School of Pharmaceutical Sciences, Osaka Medical and Pharmaceutical University, 4-20-1 Nasahara, Takatsuki, Osaka 569-1094, Japan

Published online: 19 August 2021

contributes to production of inflammatory cytokines such as TNF-α, IL-1, and IL-6 in response to lipopolysaccharide stimulation [4, 5]. p38α inhibitors have an anti-inflammatory effect and have been clinically tested as candidate therapeutic agents for rheumatoid arthritis [6]. Based on these features, non-invasive detection of aberrant p38α activity in biological tissues may be useful for precise prediction of the treatment effects of such p38α inhibitors. Nuclear medical techniques such as single photon emission computed tomography (SPECT) can be used for this purpose with targeted tracers labeled with radioisotopes such as ^{123}I, ^{111}In, and ^{99m}Tc that are suitable for use in the gamma ray energy detection range of a SPECT system [7]. However, radiometal isotopes require conjugation of a chelating moiety to the mother skeleton of a candidate lead compound that can lead to loss of function, particularly for small compounds. Here we describe the development of radioiodinated probes for use in SPECT imaging of p38α activity in inflammatory diseases.

In this study, we adopted R1487, a selective and high-affinity p38α inhibitor with a pyrimidinopyridone skeleton, as the lead compound of an imaging agent [8]. We designed the low-molecular-weight probes [^{123}I]4-I-R1487 ([^{123}I]4-IR) and [^{123}I]2-I-R1487 ([^{123}I]2-IR) in which a fluorine atom at the 4- or 2-osition of the R1487 phenoxy group was replaced with an ^{123}I atom, with a focus on the tolerability of the phenoxy moiety predicted in a previous report [8]. In whole experiments, we used ^{125}I instead of ^{123}I due to its useful radiochemical properties, such as low gamma ray energy and long half-life. We synthesized both [^{125}I]2-IR and [^{125}I]4-IR, and evaluated their effectiveness as a SPECT imaging probe that targets p38α activity in in vitro and in vivo examinations using mice treated with turpentine oil to induce inflammation.

Methods

Reagents and instruments

2-Fluoro-4-iodophenol and 4-fluoro-2-iodophenol were purchased from BLD Pharmatech (SHA, China). All other reagents were of reagent grade and were purchased from Sigma-Aldrich Japan (Tokyo, Japan), Nacalai Tesque (Kyoto, Japan), Wako Pure Chemical Industry (Osaka, Japan), or Tokyo Chemical Industry (Tokyo, Japan), and used without further purification. Melting points were measured with a Yanagimoto micro melting point apparatus (Yanaco, Kyoto, Japan). ^{1}H and ^{13}C-NMR spectra were measured using a Varian NMR system (^{1}H 400 MHz, Agilent Technologies, CA, USA) and chemical shifts are indicated as δ (ppm) values using tetramethylsilane as an internal standard. Mass spectra (MS) and high-resolution mass spectra (HRMS) were collected with a JMS-700(2)mass spectrometer (JEOL Ltd., Tokyo, Japan).

Synthesis (Scheme 1)

R1487, 2-IR, and 4-IR were synthesized following a previous report [8].

Ethyl 4-methylamino-2-methylthiopyrimidine-5-carboxylate (2)

Ethyl 4-chloro-2-ethylthiopyrimidine-5-carboxylate (**1**) (1.00 g, 4.30 mmol) was dissolved in chloroform (12.5 mL). Then, methylamine in ethanol (33%, 1.75 mL, 14.1 mmol) solution was slowly added dropwise at 0°C, and the mixture was stirred at 0°C for 30 min. After addition of 15 mL water, the solution was extracted with chloroform (15 mL × 3), and the organic layer was separated. The organic layer was dried over magnesium sulfate, filtered, and then the solution was evaporated under reduced pressure to obtain **2** as white crystals.

Yield: 95.3%. mp: 92.5–92.7°C. 1H−NMR ($CDCl_3$): 1.40 (t, J = 7.2 Hz, 3H, C$\underline{H}_3$), 2.55 (s, 3H, C$\underline{H}_3$), 2.62 (s, 3H, C$\underline{H}_3$), 4.39 (q, J = 7.1 Hz 2H, OC$\underline{H}_2$), 8.79 (s, 1H, aromatics). EI−MS: *m/z*: 227. Measured: 227.

4-Methylamino-2-methylthiopyrimidine-5-methanol (3)

Then, **2** (0.50 g, 2.2 mmol) in dry tetrahydrofuran (4.5 mL) was slowly added dropwise to lithium aluminum hydride (0.089 g, 2.4 mmol) in dry tetrahydrofuran (3.5 mL) at 5°C. The reaction mixture was stirred at 5°C for 15 min, and 0.20 mL water was slowly added dropwise. The mixture was stirred at 5°C for 30 min before 0.090 mL 15% aqueous sodium hydroxide solution was added dropwise, followed by 0.28 mL water. The mixture was stirred for 17 h at room temperature and subsequently filtered. The filter residue was washed with tetrahydrofuran (5 mL × 2), and the filtrate and washed liquid were mixed and evaporated under reduced pressure. The resulting residue was resuspended in 2:1 ethyl acetate/hexane (3 mL) solution and filtration was performed to obtain **3** as yellow crystals.

Yield: 84.0%. mp: 145.1–145.4°C. 1H−NMR ($CDCl_3$): 2.52 (s, 3H, C$\underline{H}_3$), 3.04 (d, J = 5.6 Hz, 3H, C$\underline{H}_3$), 4.49 (s, 2H, OC$\underline{H}_2$), 5.90 (s, 1H, N$\underline{H}$), 7.64 (s, 1H, aromatics), EI−MS: *m/z*: 185. Measured: 185.

4-Methylamino-2-methylthiopyrimidine-5-carboxyaldehyde (4)

3 (0.25 g, 1.4 mmol) was dissolved in chloroform (12.5 mL), and manganese dioxide (1.2 g, 1.4 mmol) was

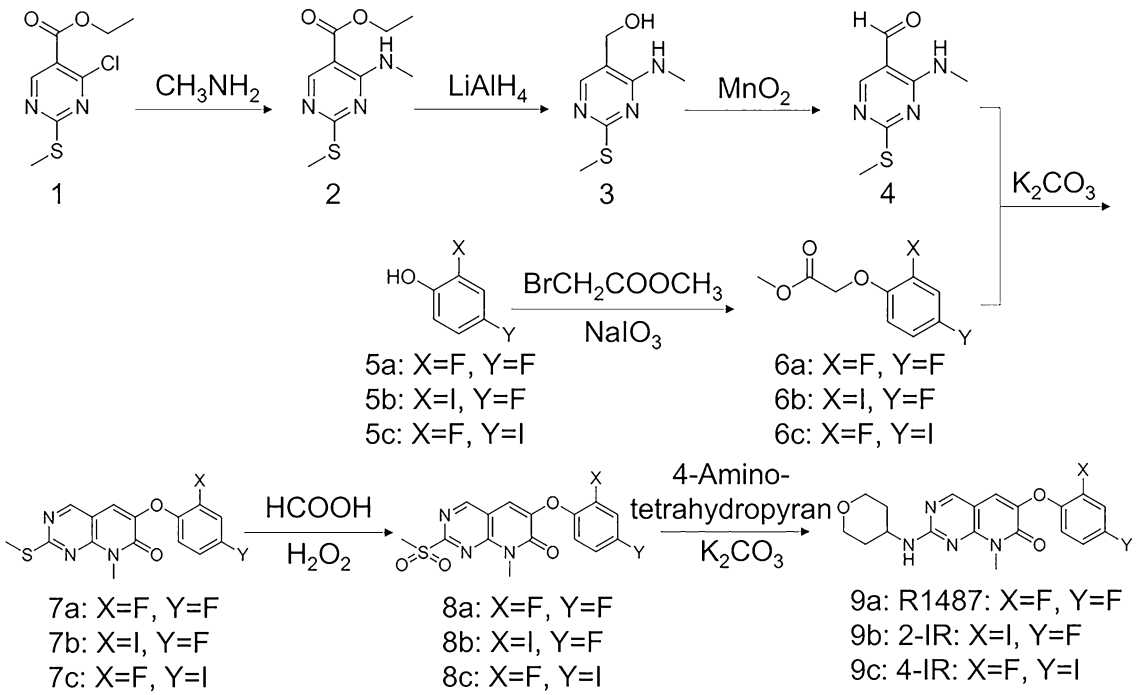

Scheme 1 Synthesis of R1487, 2-IR, and 4-IR

added with stirring. The suspension was stirred for 24 h and then evaporated to replace benzene (12.5 mL) followed by filtration through Celite. The filter residue was washed with benzene (10 mL × 5), and then the combined filtrate and wash liquid were evaporated to obtain **4** as white solids.

Yield: 73.2%. mp: 101.7–102.3°C. 1H−NMR ($CDCl_3$): 2.57 (s, 3H, C$\underline{H}_3$), 3.12 (d, J = 4.8 Hz, 3H, C$\underline{H}_3$), 8.30 (s, 1H, C$\underline{H}$O), 9.70 (s, 1H, aromatics). EI−MS: *m/z*: 183. Measured: 183.

Methyl 2-(2,4-difluorophenoxy)acetate (6a)

2,4−Difluorophenol (**5a**) (0.88 g, 6.8 mmol), methyl bromoacetate (1.1 g, 7.2 mmol), sodium iodate (6.8 mg) and potassium carbonate (1.9 g) were added in dry acetone (20 mL), and then the mixture was refluxed at 76°C for 3 h. After concentrating the mixture under reduced pressure, 25 mL water was added, the solution was extracted with chloroform (5 mL × 3), and the organic layer was separated. The organic layer was dried over sodium sulfate, and then the solution was concentrated under reduced pressure to obtain **6a** as yellow oily matter.

Yield: 93.6%. 1H−NMR ($CDCl_3$): 3.80 (s, 3H, OC$\underline{H}_3$), 4.67 (s, 2H, OC$\underline{H}_2$), 6.76–6.81 (m, 1H, aromatics), 6.85–6.97 (m, 2H, aromatics). EI−MS: *m/z*: 202. Measured: 202.

Methyl 2-(4-fluoro-2-iodephenoxy)acetate (6b)

4-Fluoro-2-iodephenol (**5b**) (0.50 g, 2.1 mmol), methyl bromoacetate (0.33 g, 2.2 mmol), sodium iodate (2.1 mg) and potassium carbonate (0.59 g) were added in dry acetone (20 mL), and then the mixture was refluxed at 76°C for 3 h. After concentrating the mixture under reduced pressure, 25 mL water was added, followed by recrystallization. Crystals were isolated to obtain **6b** as white crystals.

Yield: 92.1%. mp: 44.1–44.2°C. 1H−NMR ($CDCl_3$): 3.81 (s, 3H, OC$\underline{H}_3$), 4.76 (s, 2H, OC$\underline{H}_2$), 6.71 (dd, J = 2.4, 4.4 Hz, 1H, aromatics)), 7.01 (s, 1H, aromatics), 7.52–7.54 (m, 1H, aromatics). 13C−NMR ($CDCl_3$): 52.39, 67.04, 86.28 (d, $^2J_{C-F}$ = 8.3 Hz), 113.18 (d, $^1J_{C-F}$ = 8.4 Hz), 115.83 (d, $^1J_{C-F}$ = 22.8 Hz), 126.61 (d, $^2J_{C-F}$ = 25.0 Hz), 153.45 (d, $^3J_{C-F}$ = 2.3 Hz), 158.63 (d, J_{C-F} = 243.6 Hz), 168.76. EI−MS: *m/z*: 310. Measured: 310.

Methyl 2-(2-fluoro-4-iodephenoxy)acetate (6c)

6c was synthesized in a manner similar to that for **6b.**

Yield: 88.0%. mp: 49.0–49.3°C. 1H−NMR ($CDCl_3$): 3.80 (s, 3H, OC$\underline{H}_3$), 4.69 (s, 2H, OC$\underline{H}_2$), 6.68 (dd, J = 8.4, 8.8 Hz, 1H, aromatics), 7.36 (d, J = 10.0 Hz, 1H, aromatics), 7.42 (d, J = 12.4 Hz, 1H, aromatics). 13C−NMR ($CDCl_3$): 52.41, 66.50, 83.16 (d, $^2J_{C-F}$ = 6.8 Hz), 117.70, 125.86 (d, $^1J_{C-F}$ = 20.5 Hz), 133.41 (d, $^3J_{C-F}$ = 4.5 Hz), 146.05 (d,

$^{1}J_{C-F}$ = 10.6 Hz), 153.872 (d, J_{C-F} = 251.2 Hz), 168.67. EI−MS: *m/z*: 310. Measured: 310.

6-(2,4-Difluorophenoxy)-8-methyl-2-(methylthio)-pyrido[2,3-*d*]pyrimidin-7(8*H*)-one (7a)

4 (0.20 g, 1.1 mmol) was first dissolved in 1−methyl−2−pyrrolidinone (2 mL), and then **6a** (0.32 g, 1.6 mmol) and potassium carbonate (0.26 g) were added. The mixture was refluxed at 120°C for 12 h. In addition, **6a** (0.12 g, 0.59 mmol) and potassium carbonate (0.10 g) were added, and the mixture was refluxed at 120°C for 6 h, and then the mixture was cooled to room temperature. After 5 mL water was added, the mixture was stirred for 45 min and then filtered. The residue was washed with water (3 mL × 3) before 3 mL ethyl acetate was added. The resulting suspension was stirred for 1 h and then filtered. The residue was washed with ethyl acetate (2 mL × 3) and the residue was isolated to obtain **7a** as light-yellow crystals.

Yield: 55.6%. mp: 176.2–176.8°C. 1H−NMR ($CDCl_3$): 2.63 (s, 3H, C$\underline{H}_3$), 3.85 (s, 3H, C$\underline{H}_3$), 6.76 (s, 1H, aromatics), 6.91–6.97 (m, 1H, aromatics), 6.98–7.03 (m, 1H, aromatics), 7.16–7.23 (m, 1H, aromatics), 8.49 (s, 1H, aromatics). EI−MS: *m/z*: 335. Measured: 335.

6-(4-Fluoro-2-iodephenoxy)-8-methyl-2-(methylthio)-pyrido[2,3-*d*]pyrimidin-7(8*H*)-one (7b)

7b was synthesized in a manner similar to that for **7a**.

Yield: 57.9%. mp: 178.5–178.9°C. 1H−NMR ($CDCl_3$): 2.65 (s, 3H, C$\underline{H}_3$), 3.86 (s, 3H, C$\underline{H}_3$), 6.70 (s, 1H, aromatics), 7.05 (dd, J = 4.8, 4.8 Hz, 1H, aromatics), 7.11–7.16 (m, 1H, aromatics), 7.63 (dd, J = 2.8, 2.8 Hz, 1H, aromatics), 8.50 (s, 1H, aromatics). 13C−NMR ($CDCl_3$): 14.42, 28.65, 89.07 (d, $^{2}J_{C-F}$ = 8.4 Hz), 108.66, 113.14, 117.03 (d, $^{1}J_{C-F}$ = 22.8 Hz), 121.33 (d, $^{2}J_{C-F}$ = 8.4 Hz), 127.04 (d, $^{1}J_{C-F}$ = 25.1 Hz), 146.18, 150.73 (d, $^{3}J_{C-F}$ = 2.3 Hz), 151.54, 155.24, 158.33 (d, J_{C-F} = 21.3 Hz), 160.60, 171.37. EI−MS: *m/z*: 443 Measured: 443.

6-(2-Fluoro-4-iodephenoxy)-8-methyl-2-(methylthio)-pyrido[2,3-*d*]pyrimidin-7(8*H*)-one (7c)

7c was synthesized in a manner similar to that for **7a**.

Yield: 56.9%. mp: 181.8–182.2°C. 1H−NMR ($CDCl_3$): 2.63 (s, 3H, C$\underline{H}_3$), 3.83 (s, 3H, C$\underline{H}_3$), 6.89 (s, 1H, aromatics), 6.93 (dd, J = 8.8, 8.0 Hz, 1H, aromatics), 7.50 (d, J = 8.0 Hz, 1H, aromatics), 7.58 (d, J = 9.6 Hz, 1H, aromatics), 8.52 (s, 1H, aromatics). 13C−NMR ($CDCl_3$): 14.41, 28.59, 87.95 (d, $^{2}J_{C-F}$ = 6.9 Hz), 108.54, 113.64, 123.74, 126.54 (d, $^{1}J_{C-F}$ = 20.5 Hz), 134.29 (d, $^{3}J_{C-F}$ = 3.8 Hz), 142.05 (d, $^{1}J_{C-F}$ = 11.4 Hz), 145.79, 151.63, 152.29, 154.84 (d, J_{C-F} = 50.1 Hz), 158.27, 171.60. EI−MS: *m/z*: 443 Measured: 443.

6-(2,4-Difluorophenoxy)-8-methyl-2-(methylsulfonyl)-pyrido[2,3-*d*]pyrimidin-7(8*H*)-one (8a)

After **7a** (0.17 g, 0.51 mmol) was dissolved in chloroform (3 mL), formic acid (0.057 g, 1.24 mmol) was added, and 30% aqueous hydrogen peroxide (0.71 g, 0,63 mmol) was slowly added dropwise to the solution, which was then stirred at 38 °C. The completeness of reaction was confirmed by TLC, and the yellow solution was cooled to 25 °C before extraction with chloroform (3 mL × 3) and washing with water (0.15 mL). Additionally, the organic layer was washed with 10% aqueous NaOH solution (0.18 mL), and extracted with chloroform (3 mL × 3). The solvent was distilled off under reduced pressure. Then *tert*−butyl methyl ether (0.60 mL) was added to the residue, and the mixture was filtered and washed with *tert*−butyl methyl ether (0.20 mL × 2) at <5°C. The residue was then separated to obtain **8a** as light-yellow crystals.

Yield: 75.4%. mp: 154.2–154.7°C. 1H−NMR ($CDCl_3$): 3.40 (s, 3H, C$\underline{H}_3$), 3.95 (s, 3H, C$\underline{H}_3$), 6.78 (s, 1H, aromatics), 6.99–7.09 (m, 2H, aromatics), 7.24–7.30 (m, 1H, aromatics), 8.82 (s, 1H, aromatics). EI−MS: *m/z*: 367 Measured: 367.

6-(4-Fluoro-2-iodephenoxy)-8-methyl-2-(methylsulfonyl)-pyrido[2,3-*d*]pyrimidin-7(8*H*)-one (8b)

8b was synthesized in a manner similar to that for **8a.**

Yield: 71.8%. mp: 182.1–182.4°C. 1H−NMR ($CDCl_3$): 3.40 (s, 3H, C$\underline{H}_3$), 3.96 (s, 3H, C$\underline{H}_3$), 6.68 (s, 1H, aromatics), 7.14–7.24 (m, 2H, aromatics), 7.66 (dd, J = 2.4, 2.8 Hz, 1H, aromatics), 8.82 (s, 1H, aromatics). 13C−NMR ($CDCl_3$): 29.44, 39.32, 89.35 (d, $^{2}J_{C-F}$ = 6.2 Hz), 109.75, 115.17, 117.46 (d, $^{1}J_{C-F}$ = 15.3 Hz), 122.43 (d, $^{2}J_{C-F}$ = 12.7 Hz), 127.38 (d, $^{1}J_{C-F}$ = 16.8 Hz), 149.76 (d, $^{3}J_{C-F}$ = 4.6 Hz), 149.78, 151.86, 155.41, 159.11 (d, J_{C-F} = 145.6 Hz), 160.79, 162.82. EI−MS: *m/z*: 475 Measured: 475.

6-(2-Fluoro-4-iodephenoxy)-8-methyl-2-(methylsulfonyl)-pyrido[2,3-*d*]pyrimidin-7(8*H*)-one (8c)

8c was synthesized in a manner similar to that for **8a.**

Yield: 80.7%. mp: 110.0–110.6°C. 1H−NMR ($CDCl_3$): 3.48 (s, 3H, C$\underline{H}_3$), 4.01 (s, 3H, C$\underline{H}_3$), 6.94 (s, 1H, aromatics), 7.09 (dd, J = 8.0, 8.4 Hz, 1H, aromatics), 7.67 (d, J = 8.2 Hz, 1H, aromatics), 7.70 (d, J = 9.6 Hz, 1H, aromatics), 8.92 (s, 1H, aromatics). 13C−NMR ($CDCl_3$): 29.42, 39.31, 89.52 (d, $^{2}J_{C-F}$ = 6.9 Hz), 109.98, 115.06, 124.56, 126.89 (d, $^{1}J_{C-F}$ = 19.7 Hz), 134.79 (d, $^{3}J_{C-F}$ = 4.5 Hz), 140.69 (d, $^{1}J_{C-F}$ = 11.4 Hz), 149.44, 151.91, 152.26, 154.81 (d, J_{C-F} = 78.9 Hz), 157.60, 162.88. EI−MS: *m/z*: 475 Measured: 475.

6-(2,4-Difluorophenoxy)-8-methyl-2-(tetrahydro-2*H*-pyran-4-ylamino)pyrido[2,3-*d*]pyrimidin-7(8*H*)-one (9a: R1487)

8a, potassium carbonate and 4-aminotetrahydropyran were mixed in toluene, and the mixture was refluxed at 80°C overnight. The mixture was diluted with toluene (5 mL), and the hot suspension was filtered. The filtrate was concentrated under reduced pressure, and then the solution was cooled and the solids precipitated. The suspension was filtered and the residue was washed with water and then with 1:1 water/methanol, after which the residue was separated. The residue was recrystallized with ethanol to obtain **9a** (R1487) as white crystals.

Yield: 75.2%. mp: 177.1–177.3°C. 1H−NMR ($CDCl_3$) δ: 1.71 (s, 2H, C<u>H</u>$_2$), 2.08 (d, J = 13.2 Hz, 2H, C<u>H</u>$_2$), 3.57 (t, J = 11.0 Hz, 2H, C<u>H</u>$_2$), 3.75 (s, 3H, C<u>H</u>$_3$) 4.05 (d, J = 12.8 Hz, 2H, C<u>H</u>$_2$), 4.12 (m, 1H, C<u>H</u>), 5.30 (s, 1H, N<u>H</u>), 6.76 (s, 1H, aromatics), 6.96 (d, J = 14.6 Hz, 2H, aromatics), 7.17 (s, 1H, aromatics), 8.39 (s, 1H, aromatics).

EI−HRMS: *m/z* Calcd. for C19H18N4O3F2 [M^+]: 388.1347. Measured: 388.1351.

6-(4-Fluoro-2-iodephenoxy)-8-methyl-2-(tetrahydro-2*H*-pyran-4-ylamino)pyrido[2,3-*d*]pyrimidin-7(8*H*)-one (9b: 2-IR)

9b (2-IR) was synthesized in a manner similar to that for **9a**.

Yield: 71.8%. mp: 223.7–223.9°C. 1H−NMR ($CDCl_3$) δ: 1.61 (s, 2H, CH_2), 2.08 (d, J = 11.6 Hz, 2H, CH_2), 3.57 (m, 2H, CH_2), 3.73 (s, 3H, CH_3), 4.04 (m, J = 4.0 Hz, 2H, CH_2), 4.12 (m, J = 4.5 Hz, 1H, CH), 6.83(s, 1H, NH), 6.93 (m, J = 4.5 Hz, 1H, aromatics), 7.06 (s, 1H, aromatics), 7.59 (dd, J = 2.6 Hz, 1H, aromatics), 7.59 (dd, J = 2.6 Hz, 1H, aromatics), 8.33 (s, 1H, aromatics). 13C−NMR (DMSO−d6): 28.25, 32.95, 32.95, 47.64, 66.75, 66.75, 88.20 (d, $^2J_{C-F}$ = 9.1 Hz), 104.21, 116.49 (d, $^1J_{C-F}$ = 22.8 Hz), 117.00, 119.54 (d, $^2J_{C-F}$ = 8.4 Hz), 126.58 (d, $^1J_{C-F}$ = 25.0 Hz), 142.66, 151.74 (d, $^3J_{C-F}$ = 3.0 Hz), 153.36, 157.50, 157.54, 159.02, 160.05 (d, J_{C-F} = 6.9 Hz).

EI−HRMS: *m/z* Calcd. for C19H18N4O3FI [M^+]: 496.0408. Measured: 496.0412.

6-(4-Fluoro-2-iodephenoxy)-8-methyl-2-(tetrahydro-2*H*-pyran-4-ylamino)pyrido[2,3-*d*]pyrimidin-7(8*H*)-one (9c: 4-IR)

9c (4-IR) was synthesized in a manner similar to that for **9a**.

Yield: 50.6%. mp: 181.0–181.4°C. 1H−NMR ($CDCl_3$) δ: 1.66 (s, 2H, C<u>H</u>$_2$), 2.08 (d, J = 12.4 Hz, 2H, C<u>H</u>$_2$), 3.57 (t, J = 11.6 Hz, 2H, C<u>H</u>$_2$), 3.71 (s, 3H, C<u>H</u>$_3$), 4.02 (d, J = 12.0 Hz, 2H, C<u>H</u>$_2$), 4.11 (s, 1H, C<u>H</u>), 5.37 (s, 1H, N<u>H</u>), 6.83 (dd, J = 8.4, 8.0 Hz, 1H, aromatics), 6.98 (s, 1H, aromatics), 7.43 (d, J = 8.4 Hz, 1H, aromatics), 7.52 (s, 1H, aromatics), 8.53 (s, 1H, aromatics). 13C−NMR (DMSO−d6): 27.94, 31.72, 31.72, 47.36, 65.75, 65.75, 86.62 (d, $^2J_{C-F}$ = 20.8 Hz), 103.45, 120.13, 121.32, 125.31 (d, $^1J_{C-F}$ = 19.7 Hz), 133.83 (d, $^3J_{C-F}$ = 3.0 Hz), 140.27, 143.47 (d, $^1J_{C-F}$ = 10.6 Hz), 150.82, 153.32, 153.94 (d, J_{C-F} = 27.3 Hz), 156.62, 158.11.

EI−HRMS: *m/z* Calcd. for C19H18N4O3FI [M^+]: 496.0408. Measured: 496.0408.

Radiosynthesis (Scheme 2)

[^{125}I]Sodium iodide was purchased from PerkinElmer Japan (Kanagawa, Japan). Radioactivity levels of ^{125}I were measured with a 2480 WIZARD$^{2™}$ instrument (PerkinElmer).

6-(4-Fluoro-2-tributylstanylphenoxy)-8-methyl-2-(tetrahydro-2*H*-pyran-4-ylamino) pyrido[2,3-*d*]pyrimidin-7(8*H*)-one (10b)

2-IR, bis(tributyltin) and tetrakis(triphenylphosphine)palladium(0) were added to anhydrous toluene, and the mixture was refluxed at 140°C for 14 h before filtration through Celite. The filtrate was concentrated under reduced pressure and separated and purified by silica gel column chromatography using ethyl acetate/hexane (1/1, v/v) as an eluate to obtain **10b** as white oily matter.

Yield: 20.0%. 1H−NMR ($CDCl_3$) δ: 0.80–1.66 (m, 29H, Bu_3, C<u>H</u>$_2$), 2.08 (d, J = 11.2 Hz, 2H, C<u>H</u>$_2$), 3.57 (t, J = 10.6 Hz, 2H, C<u>H</u>$_2$), 3.73 (s, 3H, C<u>H</u>$_3$), 4.03 (d, J = 11.6 Hz, 2H, C<u>H</u>$_2$), 4.12 (m, 1H, C<u>H</u>), 5.26 (s, 1H, N<u>H</u>) 6.75 (s, 1H, aromatics), 6.84 (dd, J = 4.0, 4.0 Hz, 1H, aromatics), 6.98 (ddd, J = 3.2, 2.8, 2.8 Hz, 1H, aromatics), 7.18 (dd, J = 2.8, 2.8 Hz, 1H, aromatics), 8.28 (s, 1H, aromatics).

FAB−HRMS: *m/z* Calcd. for C31H45N4O3FSn [M+H]$^+$: 661.2576. Measured: 661.2582.

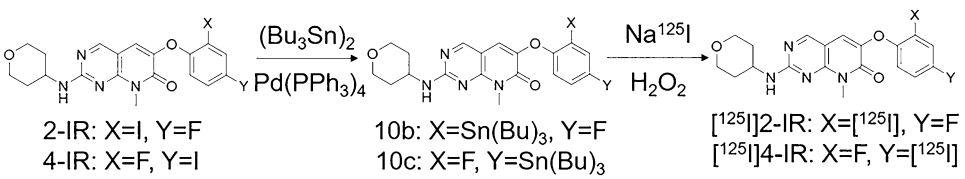

Scheme 2 Radiosynthesis of [^{125}I]2-IR and [^{125}I]4-IR

6-(2-Fluoro-4-tributylstanylphenoxy)-8-methyl-2-(tetrahydro-2*H*-pyran-4-ylamino) pyrido[2,3-*d*]pyrimidin-7(8*H*)-one (10c)

10c was synthesized in a manner similar to that for **10b**.

Yield: 90.3%. 1H−NMR ($CDCl_3$) δ: 0.88–1.65 (m, 29H, Bu_3, C$\underline{H}_2$), 2.08 (d, J = 11.2 Hz, 2H, C$\underline{H}_2$), 3.57 (t, J = 10.8 Hz, 2H, C$\underline{H}_2$), 3.74 (s, 3H, C$\underline{H}_3$), 4.02 (d, J = 11.2 Hz, 2H, C$\underline{H}_2$), 4.11 (s, 1H, C$\underline{H}$), 5.33 (s, 1H, N$\underline{H}$) 6.83 (s, 1H, aromatics), 7.01 (dd, J = 7.6, 7.6 Hz, 1H, aromatics), 7.18 (d, J = 6.8 Hz 1H, aromatics), 7.25 (d, J = 6.8 Hz 1H, aromatics), 8.31 (s, 1H, aromatics).

EI−HRMS: *m/z* Calcd. for C31H45N4O3FSn [M^+]: 660.2498. Measured: 660.2504.

6-(4-Fluoro-2-[^{125}I]iodephenoxy)-8-methyl-2-(tetrahydro-2H-pyran-4-ylamino)-pyrido[2,3-d]pyrimidin-7(8H)-one ([^{125}I]2-IR)

10b (10 µL, 1 mg/mL ethanol solution), 0.1 M HCl solution (100 µL), [^{125}I] sodium iodide (0.2 µL, 7.4 MBq), and 5% aqueous hydrogen peroxide (10 µL) were mixed in a sealed vial, and then the mixture was shaken and stirred at room temperature for 15 min. After the mixture was filtered with a 4 mm Cosmonice Filter W (Aqueous; Nacalai Tesque), the target compound was purified by a reverse-phase HPLC composed of two pumps (LC-20AT, Shimadzu, Kyoto, Japan), an absorbance detector (SPD-20A, Shimadzu), a 170 type I radioactivity detector (Beckman Coulter, CA, USA), and a Cosmosil 5C18-AR-II column (10 × 250 mm, Nacalai Tesque). A mobile phase of methanol/water (75/25, v/v) at a flow rate of 3 mL/min was used. Subsequently, 2-IR and [^{125}I]2-IR were spotted on TLC Silica gel 60 F254 TLC plates (Aluminum Sheet 20 × 20 cm; Merck, Darmstadt, Germany) and simultaneouslydeveloped with chloroform/methanol (30/1). After the unlabeled 2-IR spot was detected on the TLC plate under illumination at 254 nm, the plate was divided into 10 regions, and the radioactivity in each region was measured. The radiochemical purity was estimated as the percentage of the radioactivity in a given region of the plate relative to the total radioactivity.

6-(2-Fluoro-4-[^{125}I]iodephenoxy)-8-methyl-2-(tetrahydro-2H-pyran-4-ylamino)-pyrido[2,3-d]pyrimidin-7(8H)-one ([^{125}I]4-IR)

[^{125}I]4-IR was synthesized in a manner similar to that for [^{125}I]2-IR.

Measurement of Log *D* values

Log *D* values of [^{125}I]2-IR and [^{125}I]4-IR were measured as previously described [9]. In brief, [^{125}I]2-IR (52.0 kBq) and [^{125}I]4-IR (47.1 kBq) were added to a mixture of 1−octanol and PBS (−) (pH = 7.4), stirred with shaking, and centrifuged. Then, the liquid was collected from each liquid layer, the radioactivity was measured, and the log *D* value was calculated.

In vitro kinase inhibition assay

The kinase inhibitory activities of 2-IR, 4-IR, R1487, and SB203580 (AdooQ BioScience, CA, USA) were measured using an ADP-Glo™ kinase assay system (Promega, MSN, USA) according to the method recommended by Promega. Briefly, the test compound (2-IR, 4-IR, or SB203580, final concentration of 1 nM−100 µM; R1487, final concentration of 0.033 nM−3.3 µM), active p38α, p38 substrate, and 150 mM ATP included in the assay solution were mixed and incubated at room temperature for 60 min. The ADP-Glo™ reagent was added to the solution and incubated at room temperature for 40 min. A kinase detection reagent was then added and incubated at room temperature for another 30 min. Finally, the luminescence was measured with a Hidex Sense Beta Photometer (Hidex, Turku, Finland) with an integration time of 1 s. The inhibition activity of the tested compounds was evaluated by determining the 50% inhibitory potency (IC_{50}) from inhibition curves.

Preparation of turpentine oil-induced inflammation model mice

The animal experiments in this study were conducted in accordance with Osaka University of Pharmaceutical Sciences guidelines for experiments involving animals. The study protocol was approved by the Experimental Animal Committee at Osaka University of Pharmaceutical Sciences (Permission Number: 18–76, 19–76, and 20–76). Male ddY mice (4 weeks old) were purchased from Japan SLC (Shizuoka, Japan) and allowed access to food and water ad libitum. Animals were given intramuscular injections with turpentine oil (50 µL) in the left thigh region under isoflurane anesthesia and used for experiments 2 days after the injection. Muscle from contralateral untreated regions of the same mouse was used as the untreated control.

In vitro stability analysis

[^{125}I]2-IR (10 µL, 27.7 kBq), and [^{125}I]4-IR (10 µL, 18.3 kBq) were incubated in ddY mice plasma (100 µL) for 0, 1, 2, 6, and 24 h at 37 °C. Methanol was then added and the mixture was centrifuged. The resulting supernatant was analyzed in a manner similar to that used for radiochemical purity analysis. The intact rate (%) was calculated as the percentage of the radioactivity detected in the intact form region relative to the total radioactivity.

Western blotting analysis

Inflamed and contralateral uninflamed muscle tissues were excised from inflammation model mice ($n = 3$), homogenized in Passive Lysis Buffer (Promega) and centrifuged to remove debris. After determining the protein concentration of the samples using the Pierce BCA Protein Assay Kit (Thermo Scientific, MA, USA) and measuring the absorbance at 562 nm with a Hidex Sense Beta Photometer (Hidex), the samples were diluted with sample buffer containing dithiothreitol to a protein concentration of 0.2 mg/mL. The samples (5 µL) were then loaded onto a polyacrylamide gel and western blotting was performed using human/mouse/rat p38 alpha antibody (0.4 µg/mL, AF8691, R&D Systems, MSP, USA) and phospho-p38 MAPK (Thr180, Tyr182) polyclonal antibody (1:1000 dilution, 36–8500, Invitrogen, CA, USA) as the primary antibodies and rabbit IgG HRP−conjugated antibody (1:3000 dilution, HAF008, R&D systems) as the secondary antibody. GAPDH levels in the samples were used as protein loading controls and were measured with rabbit polyclonal GAPDH antibody (GeneTex, GTX110118, LAX, USA). Immunoreactive bands were visualized using Chemi−Lumi One Ultra (Nacalai Tesque). The FastGene Bluestar prestained protein marker (NIPPON genetics, Tokyo, Japan) was used as a molecular weight marker to estimate molecular weights. An Amersham Imager 600 (GE Healthcare Japan, Tokyo, Japan) was used to visualize bands on the western blot.

Biodistribution study

[^{125}I]2-IR (23.9–28.9 kBq/100 µL saline containing 0.2% Tween 80) and [^{125}I]4-IR (17.1–19.0 kBq/100 µL saline containing 0.2% Tween 80) were intravenously injected into ddY mice and inflammation model mice. The mice were sacrificed under isoflurane anesthesia at 5, 15, 30, 60, or 120 min ($n = 4$ for each time point) after probe administration. The inflamed site was carefully identified by appearance such as abscess, color, and hardness. Samples of inflamed tissue and tissues of interest were excised for measurement of weight and radioactivity. Radioactivity accumulation in the tissues is expressed in terms of the percentage of the injected dose per gram of tissue (%ID/g).

In vivo inhibition study

Radioactivity accumulation in the inflamed tissue and normal muscle 30 min after intravenous injection of [^{125}I]4-IR (17.2 kBq/100 µL saline containing 0.2% Tween 80) in inflammation model mice ($n = 3$ each) was measured with or without intraperitoneal injection of saline containing 0.2% Tween 80 and R1487 (30 mg/kg) or ralimetinib (30 mg/kg, Selleck Chemicals, TX, USA) 60 min prior to the probe administration.

Statistical analysis

Data are shown as means ± standard deviations (S.D.). Statistical analysis was performed with GraphPad Prism 8 using Tukey's multiple comparison test for in vitro kinase inhibition assay analysis and in vivo inhibition study analysis, and paired t test for western blotting analysis. A two-tailed value of $p < 0.05$ was considered as statistically significant.

Results

Synthesis (Scheme 1)

We designed and synthesized two pyrimidinopyridone derivatives, 2-IR and 4-IR, based on the structure of R1487, a well−characterized selective p38α inhibitor. In the first route, **1** was reacted with methylamine to obtain **2**, which was subsequently reduced with $LiAlH_4$ to obtain **3**, and then oxidized using MnO_2 to obtain **4**. In another route, **5a−c** was reacted with methyl bromoacetate to obtain **6a−c** according to a previously reported method [10]. Next, **4** and **6a−c** were condensed to obtain **7a−c**, which was then oxidized with performic acid to obtain **8a−c** having a sulfone group that was displaced with 4−aminotetrahydropyran to obtain **9a** (R1487), **9b** (2-IR), and **9c** (4-IR). R1487, 2-IR, and 4-IR were synthesized at total yields of 24.2%, 17.5%, and 19.2%, respectively.

In vitro kinase inhibition assay

The IC_{50} values of the tested compounds were determined (Table 1). The IC_{50} values were 139.4 ± 26.5 nM and 88.9 ± 14.5 nM for 2-IR and 4-IR, respectively, indicating a significantly lower potency of both compounds relative to R1487 (11.8 ± 8.3 nM); however, 4-IR exhibited significantly

Table 1 IC_{50} values of 4-IR, 2-IR, and p38α inhibitors

Compound	IC_{50} (nM)
2-IR	139.4 ± 26.5*†
4-IR	88.9 ± 14.5†
R1487	11.8 ± 8.3*
SB203580	142.2 ± 33.1*†

Data represent mean ± SD, $n = 5$

*$p < 0.05$ vs. 4-IR

†$p < 0.05$ vs. R1487

higher potency than the p38α inhibitor SB203580 (142.2 ± 33.1 nM).

Radiosynthesis (Scheme 2)

Radioiodination of 2-IR and 4-IR was performed via an organotin–radioiodine exchange reaction using the corresponding tributyltin precursors. After an initial HPLC purification, on analytical HPLC, [^{125}I]2-IR and [^{125}I]4-IR radioactivity had retention times of 11.1 min and 14.3 min, respectively, which coincided with the retention times of nonradioactive 2-IR and 4-IR as detected by UV absorbance. The radiochemical yield and radiochemical purity for [^{125}I]2-IR were 65.6% and 99.7%, respectively, whereas those for [^{125}I]4-IR were 84.2% and 97.5%. The molar activities for both were estimated to be 81 GBq/μmol. The log *D* values were 2.50 ± 0.05 and 2.10 ± 0.02 for [^{125}I]2-IR and [^{125}I]4-IR, respectively.

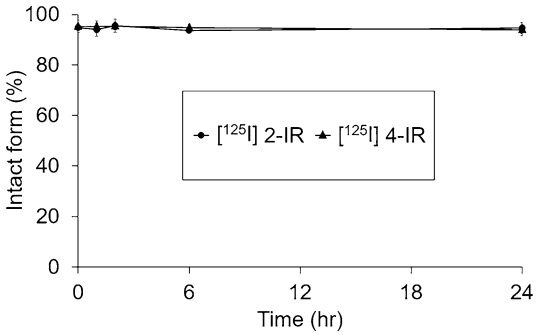

Fig. 1 In vitro stability of [^{125}I]2-IR and [^{125}I]4-IR in plasma. Data represent mean ± SD, $n = 4$

In vitro stability analysis

The intact percentages after incubation of [^{125}I]2-IR and [^{125}I]4-IR in mouse plasma were shown in Fig. 1. Both [^{125}I]2-IR and [^{125}I]4-IR were highly stable in mouse plasma for 24 h.

Preparation of turpentine oil-induced inflammation model mice

Inflammation model mice were prepared by intramuscular injection of turpentine oil in male ddY mice. Expression levels of p-p38α and phosphorylated p38α (p-p38α) proteins in inflamed muscle from the treated area and muscle from an unaffected area from the same mouse were evaluated by western blotting (Fig. 2, Supplementary Fig. 1). The p38α/GAPDH ratios were comparable between the inflamed and untreated muscle (Fig. 2b), whereas the p-p38α/GAPDH ratio was significantly higher in inflamed than uninflamed muscle (Fig. 2c).

Biodistribution study

The biodistribution of [^{125}I]2-IR and [^{125}I]4-IR was first evaluated in normal ddY mice (Supplementary Tables 1 and 2). Both probes showed a similar biodistribution profile characterized by fast radioactivity delivery and clearance throughout the body, except for the small intestine and the colon, which are recognized as major excretion routes for

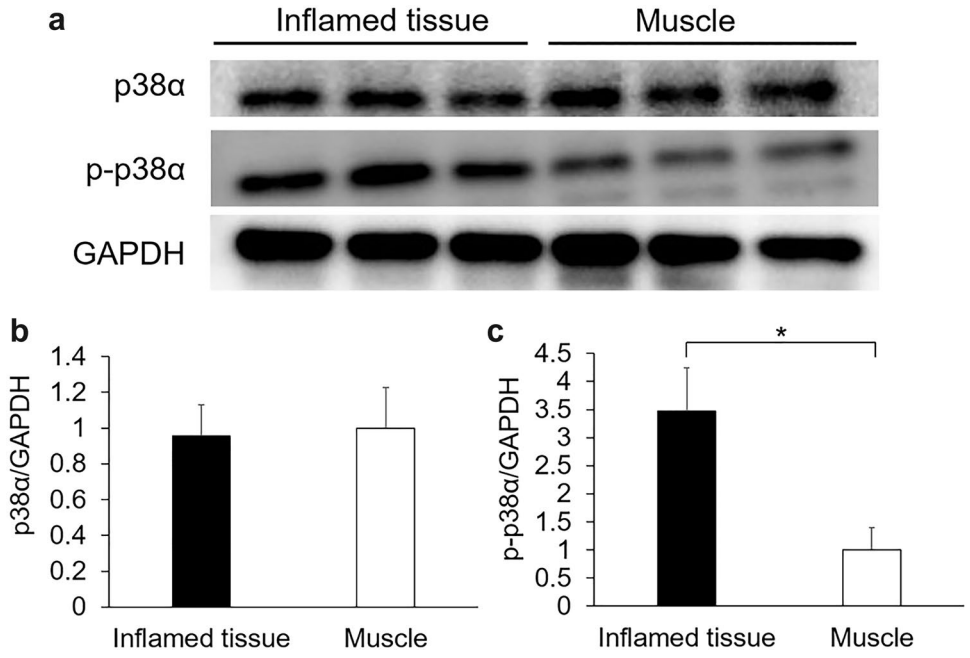

Fig. 2 Protein expression levels of p38α in muscle tissue. **a** Representative western blot bands for p38α, p-p38α, and GAPDH in homogenates of inflamed and uninflamed muscle tissue from different gels. Expression of **b** p38α and **c** p-p38α in the inflammation compared with muscle expression corrected to 1 after normalization to GAPDH. Data represent mean ± SD, $n = 3$ *$p < 0.05$

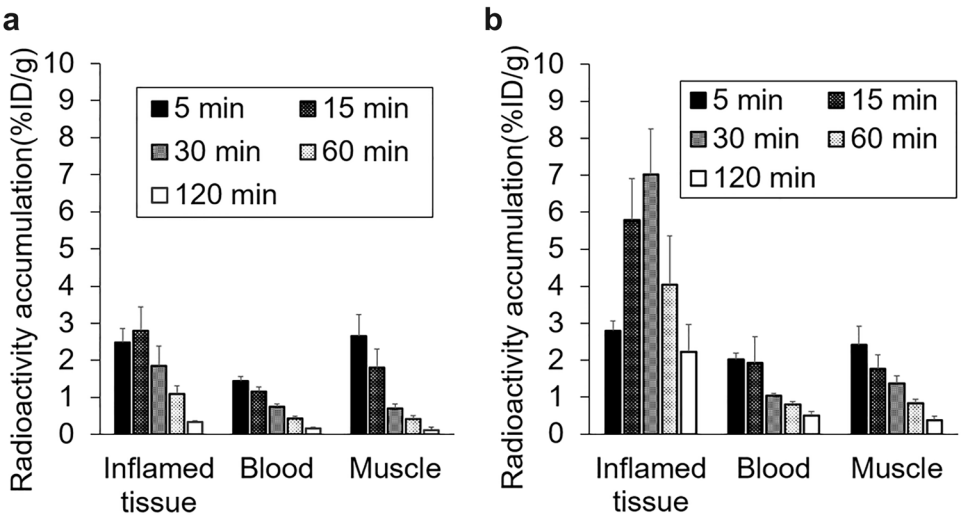

Fig. 3 Biodistribution of probes in inflammation model mice. In vivo biodistribution of **a** [^{125}I]2-IR and **b** [^{125}I]4-IR in inflammation model mice. Data represent mean %ID/g ± SD, $n = 4$

Table 2 In vivo biodistribution of [^{125}I]2-IR in inflammation model mice

	Time after injection (min)				
	5	15	30	60	120
Inflamed tissue	2.5 ± 0.4	2.8 ± 0.6	1.8 ± 0.5	1.1 ± 0.2	0.3 ± 0.0
Blood	1.4 ± 0.1	1.2 ± 0.1	0.7 ± 0.1	0.4 ± 0.1	0.2 ± 0.0
Pancreas	5.2 ± 0.4	3.3 ± 0.6	1.2 ± 0.2	0.6 ± 0.1	0.3 ± 0.0
Spleen	2.9 ± 0.3	2.0 ± 0.3	0.7 ± 0.1	0.4 ± 0.1	0.2 ± 0.1
Stomach*	1.3 ± 0.6	5.3 ± 3.0	2.1 ± 0.6	3.0 ± 1.1	2.3 ± 0.4
Small intestine	5.2 ± 0.8	8.0 ± 2.6	15.7 ± 4.7	27.1 ± 2.5	28.3 ± 8.3
Colon	1.8 ± 0.3	2.0 ± 0.4	2.0 ± 0.3	4.0 ± 2.1	18.8 ± 13.1
Liver	11.6 ± 0.8	8.2 ± 0.7	4.7 ± 0.5	4.6 ± 1.1	2.3 ± 1.2
Kidney	6.3 ± 0.3	4.5 ± 0.5	3.3 ± 0.4	2.4 ± 0.2	1.0 ± 0.2
Heart	4.4 ± 0.6	2.6 ± 0.5	1.1 ± 0.1	0.6 ± 0.1	0.2 ± 0.1
Lung	4.1 ± 0.8	2.8 ± 0.3	1.1 ± 0.2	0.7 ± 0.3	0.3 ± 0.1
Thyroid*	0.0 ± 0.0	0.0 ± 0.0	0.0 ± 0.0	0.0 ± 0.0	0.0 ± 0.0
Muscle	2.7 ± 0.4	1.8 ± 0.2	0.7 ± 0.1	0.4 ± 0.1	0.1 ± 0.0
Bone	1.7 ± 0.6	1.0 ± 0.2	0.3 ± 0.0	0.3 ± 0.2	0.1 ± 0.0
Brain	2.7 ± 0.3	1.4 ± 0.2	0.5 ± 0.0	0.2 ± 0.0	0.1 ± 0.0

Data represent mean %ID/g ± SD, $n = 4$

*Data represent mean %ID ± SD, $n = 4$

Table 3 In vivo biodistribution of [^{125}I]4-IR in inflammation model mice

	Time after injection (min)				
	5	15	30	60	120
Inflamed tissue	2.8 ± 0.3	5.8 ± 1.1	7.0 ± 1.2	4.0 ± 1.3	2.2 ± 0.7
Blood	2.0 ± 0.2	1.9 ± 0.7	1.0 ± 0.1	0.8 ± 0.1	0.5 ± 0.1
Pancreas	4.7 ± 0.7	3.5 ± 0.3	2.1 ± 0.3	1.3 ± 0.2	0.8 ± 0.1
Spleen	2.4 ± 0.3	1.9 ± 0.1	1.3 ± 0.1	0.8 ± 0.1	0.4 ± 0.1
Stomach*	1.3 ± 0.1	1.9 ± 0.2	3.5 ± 0.4	3.8 ± 1.0	3.9 ± 1.7
Small intestine	4.1 ± 0.4	7.4 ± 0.3	14.5 ± 2.7	23.1 ± 1.5	24.8 ± 2.1
Colon	1.6 ± 0.2	2.0 ± 0.1	2.3 ± 0.1	3.6 ± 0.5	16.5 ± 4.4
Liver	10.7 ± 1.0	8.1 ± 0.9	5.3 ± 0.5	3.7 ± 0.6	2.9 ± 0.9
Kidney	6.0 ± 1.1	4.6 ± 0.5	3.5 ± 0.3	2.3 ± 0.2	1.4 ± 0.3
Heart	3.9 ± 0.5	3.0 ± 0.4	1.7 ± 0.2	1.2 ± 0.1	0.5 ± 0.1
Lung	3.7 ± 0.3	3.1 ± 0.4	1.8 ± 0.1	1.2 ± 0.1	0.7 ± 0.1
Thyroid*	0.0 ± 0.0	0.0 ± 0.0	0.0 ± 0.0	0.0 ± 0.0	0.0 ± 0.0
Muscle	2.4 ± 0.4	1.8 ± 0.2	1.4 ± 0.1	0.8 ± 0.1	0.4 ± 0.1
Bone	1.2 ± 0.1	1.2 ± 0.2	0.7 ± 0.1	0.6 ± 0.1	0.2 ± 0.1
Brain	2.8 ± 0.4	1.7 ± 0.2	1.0 ± 0.2	0.6 ± 0.0	0.3 ± 0.0

Data represent mean %ID/g ± SD, $n = 4$

*Data represent mean %ID ± SD, $n = 4$

such lipophilic compounds. In particular, the low and negligible radioactivity levels detected in the stomach and the thyroid, respectively, indicated high stability against deiodination reactions in vivo.

Biodistribution of [^{125}I]2-IR and [^{125}I]4-IR were next investigated in the inflammation model mice (Fig. 3, Tables 2 and 3). The radioactivity accumulation in the inflamed tissue after [^{125}I]4-IR administration peaked at 30 min post-injection (7.0 ± 1.2%ID/g) and then gradually decreased to 2.2 ± 0.7%ID/g at 2 h post-injection. In addition, radioactivity levels in the blood and muscle were low and rapidly cleared, which resulted in a high inflammation-to-blood ratio (6.2 ± 0.4) and a high inflammation-to-muscle ratio (5.2 ± 1.3) observed 30 min post-injection. In contrast, radioactivity accumulation in inflamed tissue after [^{125}I]2-IR administration peaked at 15 min post−injection (2.8 ± 0.6%ID/g) and then gradually decreased to 0.3 ± 0.0%ID/g at 2 h post-injection. For this probe, the inflammation-to-blood ratio and inflammation-to-muscle ratio at 15 min post−injection were 2.4 ± 0.5 and 1.6 ± 0.4, respectively.

In vivo inhibition study

Mice were first treated or not with R1487 or ralimetinib delivered by intraperitoneal injection. At 60 min after administration, [^{125}I]4-IR was delivered and 30 min later samples of inflamed and uninflamed muscle tissue were taken. The accumulation of radioactivity in the inflamed tissue was significantly decreased by systemic pretreatment with both p38α inhibitors, while levels in the uninflamed muscle were not affected (Fig. 4).

Discussion

In this study, we designed the probes [^{123}I]2-IR and [^{123}I]4-IR based on the pyrimidinopyridone structure of a potent p38α-selective inhibitor, R1487, as an activated p38α imaging probe for SPECT, synthesized radiolabeled compounds using an easy-to-use radioiodine-125 ([^{125}I]2-IR and [^{125}I]4-IR) instead of radioiodine-123, and evaluated the usefulness of each compound in in vitro and in vivo experiments. 4-IR showed significantly higher inhibitory activity toward p38α relative to 2-IR and SB203580. In particular, [^{125}I]4-IR exhibited high radioactivity accumulation in inflamed tissue, depending on the levels of p-p38α expression, as well as favorable pharmacokinetic characteristics, such as rapid delivery and clearance and high stability. These results indicated that [^{123}I]4-IR, in particular, is a promising imaging probe for use with SPECT to identify regions having high p-p38α expression that would occur in a variety of inflammatory diseases.

p38α is an intracellular signaling kinase that is ubiquitously expressed in mammalian cells [3]. This kinase is known to be activated in response to a variety of external stimuli such as inflammatory cytokines [2], lipopolysaccharide [5], and osmotic shock [1]. In this study, we used mice treated with turpentine oil as a model of inflammation. We confirmed high expression levels of the active form of p38α, p-p38α, in inflamed lesions that arose following treatment compared to normal, untreated muscle, which verifies that this animal model of inflammation is relevant for testing these probes. p-p38α is p38α phosphorylated at residues Thr180/Tyr182 by MAP kinase kinases. Since R1487 and ralimetinib both bind to an ATP-binding site in p-p38α [8, 11] that is covered by a crossover connection in a naive p38α prior to phosphorylation of these two residues [12], it is suggested that [^{125}I]2-IR and [^{125}I]4-IR can bind to the ATP-binding site of p-p38α and thus would be valuable probes to detect sites with disease activity as evidenced by high p-p38α expression levels.

R1487 was selected as the parent compound for the radiotracer in this study based on its high affinity and selectivity toward activated p38α [8], as well as the strong interaction between the R1487 pyrimidinopyridone moiety and the ATP-binding site (Thr106-Gly110) of p-p38α [8]. We predicted that the residual phenoxy group could be used as an imaging moiety after the introduction of radioiodine-123. Moreover, the phenoxy group also contributes to the preferential recognition of p38α compared to p38β [8]. The two R1487 derivatives having phenoxy group fluorination at positions 2- or 4- showed similar selectivity [8]. As such, we tested the performance of both 2- or 4-radioiodinated R1487 tracers.

We observed a significant decrease in inhibitory potency for both 2-IR and 4-IR relative to unmodified R1487, and 4-IR had reduced specificity between p38α/p38β

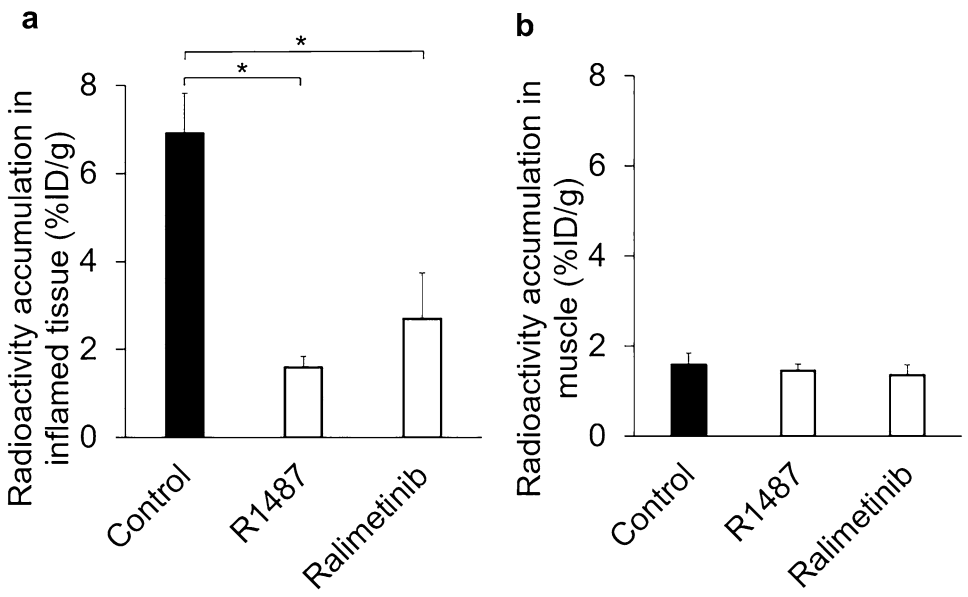

Fig. 4 In vivo inhibition of [^{125}I]4-IR radioactivity accumulation in **a** inflamed tissue and **b** muscle using p38α selective inhibitors. Data represent mean %ID/g ± SD, $n = 3$ *$p < 0.05$

(Supplementary Fig. 2). These results indicate that the phenoxy moiety makes a clear contribution to the p38α interaction and that the introduction of a large atom like iodine in the phenoxy group could produce steric hinderance at amino acid residues that comprise the ATP-binding pocket that in turn affects interactions with and recognition of p-p38α [8].

The in vivo biodistribution study could clearly differentiate radioactivity accumulation profiles for [^{125}I]2-IR and [^{125}I]4-IR in inflamed tissue. [^{125}I]4-IR showed cumulative radioactivity accumulation in the inflamed tissue over the first 30 min, accompanied by a monotonic decrease in blood radioactivity that suggests strong active targeting of the probe toward p-p38α in the inflamed tissue. This result is likely associated with the significant difference in the inhibition potency of the two probes, given that the physicochemical characteristics are similar, as is the biodistribution profile in normal mice. Based on a previously reported docking simulation, we hypothesized that the fluorine at positions 2- and 4- of the R1487 phenoxy ring can both be replaced by a large atom such as iodine without having a significant effect on the inhibitory potency [8]. However, the results of this study indicate that replacement of fluorine with iodine at the 2-position produces more steric hindrance compared to the 4-position. The in vivo biodistribution study of [^{125}I]4-IR showed not only high radioactivity accumulation in the inflamed tissue, but also high inflammation-to-blood and inflammation-to-muscle ratios (indices for in vivo imaging with SPECT) within 1 h post-injection of the tracer. Accumulation levels were similar to those observed for 2-[^{18}F]fluoro-2-deoxy-D-glucose ([^{18}F]FDG), a well-known inflammation imaging tracer [13], obtained in the same inflammation model mice (Supplementary Fig. 3). While [^{18}F]FDG has been widely used as an inflammation imaging agent, [^{18}F]FDG also accumulates in normal brain, heart, and cramped and post-exercise muscles, leading to difficulty in detecting inflamed tissues in images [14]. These findings, along with the results of the present study, may support the development of other imaging agents based on different accumulation mechanisms, such as the p38 MAPK pathway investigated in this study. Together the in vivo results suggest that [^{123}I]4-IR would be a valuable probe for in vivo SPECT imaging of p-p38α in a variety of disease settings.

As already mentioned above, naive p38α is ubiquitously expressed in mammalian cells [3] and phosphorylated to become active p38α in response to external stimuli. Therefore, in vivo imaging targeting the p38α pathway in disease pathology may be achieved by the development of an imaging probe that is specific for the activated form of p38α. The radioiodinated probe [^{125}I]m-YTM previously reported by our group, which is the only p38α probe that has been developed to our knowledge, targeted total p38α, including both naive and activated forms [15], indicating limited utility as an imaging probe for p38α activation in disease states. In contrast, [$^{123/125}$I]4-IR designed using R1487, which specifically binds to activated p38α, exhibits superior potential as an imaging probe targeting biological functions of the p38α pathway activated in disease settings, compared to [^{125}I]m-YTM.

Activation of p38α contributes not only to inflammatory responses, but also to regulation of several pathological functions, such as angiogenesis [16–18] and apoptosis [19, 20]. Therefore, activated p38α imaging with [^{123}I]4-IR could be versatile enough to be applied to cancer and atherosclerosis, and of worth to be evaluated using other various disease model animals in the future, aside from the turpentine oil-induced inflammation model mice used in this study. Considering the sensitivity of [^{123}I]4-IR for inflammatory disease imaging, comparable radioactivity accumulation in the inflamed tissue with that observed for [^{18}F]FDG in the model mice suggests the potential use of [^{123}I]4-IR for this purpose. We used model mice recognized as an acute inflammation animal model mainly due to the utility and high degree of expression of activated p38α. Because several other cascades relevant to NF-κB [21] and JNK [22] are also involved in the inflammatory response, in addition to the p38α pathway, careful evaluation is required in future studies to determine the utility of [^{123}I]4-IR in other pathological disease model animals.

This study does have some limitations. The inhibitory activity of 4-IR was about 10 times significantly lower than that of R1487, although it was still significantly higher than that of the p38α inhibitor SB203580. The diminished selectivity of 4-IR for p38α over p38β compared to R1487 should also be addressed. As mentioned above, the introduction of a large atom like iodine at the 4-position of the R1487 phenoxy moiety could affect the binding affinity due to steric hindrance. Introduction of radiofluorine-18 instead of radioiodine-123/125 at the 4-position could address this issue, considering recent reports concerning direct ^{18}F labelling of a benzene ring from corresponding boronic acid pinacol ester [23–25] or tributylstannyl [26, 27] precursors. [^{18}F]R1487 obtained using the direct radiofluorination reaction could preserve the binding profile of the mother compound R1487 and would still allow for positron emission tomography (PET) imaging applications. We are currently pursuing development of [^{18}F]R1487 for p-p38α PET imaging.

In summary, [^{125}I]4-IR newly designed as an activated p38α targeting probe could be synthesized with high radiochemical yield, purity, and molar activity. [^{125}I]4-IR showed high inhibitory activity toward p38α, high stability, and favorable pharmacokinetic characteristics, such as high radioactivity accumulation in inflamed tissue and rapid blood clearance in a mouse model of inflammation. Together, [^{123}I]4-IR can target areas with high p-p38α expression and thus could be a valuable probe for use with SPECT imaging of various inflammatory diseases.

Supplementary Information The online version contains supplementary material available at https://doi.org/10.1007/s12149-021-01669-6.

Acknowledgements We are grateful for the technical assistance of Ms. Atsuko Takeguchi, Ms. Kaede Hanazono, Mr. Ryuji Kakisaka, Mr. Naofumi Yoshida, and Ms. Nami Nakai.

Author contributions TH, MH, and TT conceptualized and designed the study. TH, NK, and MH performed the experiments and collected the data. TH, NK, MH, and TT interpreted the data. TH drafted the initial manuscript, which was critically reviewed by NK and TT. All authors approved the final manuscript and are accountable for all of the work.

Funding This work was supported in part by JSPS KAKENHI (19H03606).

Declarations

Conflict of interest All authors declare no conflicts of interests. The funding bodies had no role in study design, data collection and analysis, decision to publish, or manuscript preparation.

References

1. Cohen DM. Mitogen-activated protein kinase cascades and the signaling of hyperosmotic stress to immediate early genes. Comp Biochem Physiol A Physiol. 1997;117(3):291–9.
2. Johnson GL, Lapadat R. Mitogen-activated protein kinase pathways mediated by ERK, JNK, and p38 protein kinases. Science. 2002;298(5600):1911–2.
3. Ono K, Han J. The p38 signal transduction pathway: activation and function. Cell Signal. 2000;12(1):1–13.
4. Lee JC, Laydon JT, McDonnell PC, Gallagher TF, Kumar S, Green D, et al. A protein kinase involved in the regulation of inflammatory cytokine biosynthesis. Nature. 1994;372(6508):739–46.
5. Beyaert R, Cuenda A, Vanden Berghe W, Plaisance S, Lee JC, Haegeman G, et al. The p38/RK mitogen-activated protein kinase pathway regulates interleukin-6 synthesis response to tumor necrosis factor. Embo j. 1996;15(8):1914–23.
6. Cohen SB, Cheng TT, Chindalore V, Damjanov N, Burgos-Vargas R, Delora P, et al. Evaluation of the efficacy and safety of pamapimod, a p38 MAP kinase inhibitor, in a double-blind, methotrexate-controlled study of patients with active rheumatoid arthritis. Arthritis Rheum. 2009;60(2):335–44.
7. Khalil MM, Tremoleda JL, Bayomy TB, Gsell W. Molecular SPECT imaging: an overview. Int J Mol Imaging. 2011;2011:796025.
8. Goldstein DM, Soth M, Gabriel T, Dewdney N, Kuglstatter A, Arzeno H, et al. Discovery of 6-(2,4-difluorophenoxy)-2-[3-hydroxy-1-(2-hydroxyethyl)propylamino]-8-methyl-8*H*-pyrido[2,3-*d*]pyrimidin-7-one (Pamapimod) and 6-(2,4-difluorophenoxy)-8-methyl-2-(tetrahydro-2*H*-pyran-4-ylamino)pyrido[2,3-*d*]pyrimidin-7(8*H*)-one (R1487) as orally bioavailable and highly selective inhibitors of p38α mitogen-activated protein kinase. J Med Chem. 2011;54(7):2255–65.
9. OECD. Test No. 107: Partition Coefficient (n-octanol/water): Shake Flask Method. 1995.
10. RamaRao VV, Reddy GV, Maitraie D, Ravikanth S, Yadla R, Narsaiah B, Rao PS. One-pot synthesis of fluorine containing 3-cyano/ethoxycarbonyl-2-methyl-benzo[*b*]furans. Tetrahedron. 2004;60(52):12231–7.
11. Campbell RM, Anderson BD, Brooks NA, Brooks HB, Chan EM, De Dios A, et al. Characterization of LY2228820 dimesylate, a potent and selective inhibitor of p38 MAPK with antitumor activity. Mol Cancer Ther. 2014;13(2):364–74.
12. Zhang YY, Wu JW, Wang ZX. Mitogen-activated protein kinase (MAPK) phosphatase 3-mediated cross-talk between MAPKs ERK2 and p38alpha. J Biol Chem. 2011;286(18):16150–62.
13. Pellegrino D, Bonab AA, Dragotakes SC, Pitman JT, Mariani G, Carter EA. Inflammation and infection: imaging properties of ^{18}F-FDG-labeled white blood cells versus ^{18}F-FDG. J Nucl Med. 2005;46(9):1522–30.
14. Parida GK, Roy SG, Kumar R. FDG-PET/CT in skeletal muscle: pitfalls and pathologies. Semin Nucl Med. 2017;47(4):362–72.
15. Hirata M, Yao T, Fujimura S, Kanai Y, Yoshimoto M, Sato T, et al. Development of a p38α-selective radioactive probe for qualitative diagnosis of cancer using SPECT. Ann Nucl Med. 2019;33(5):333–43.
16. Patnaik A, Haluska P, Tolcher AW, Erlichman C, Papadopoulos KP, Lensing JL, et al. A first-in-human phase I study of the oral p38 MAPK inhibitor, Ralimetinib (LY2228820 Dimesylate), in patients with advanced cancer. Clin Cancer Res. 2016;22(5):1095–102.
17. Leelahavanichkul K, Amornphimoltham P, Molinolo AA, Basile JR, Koontongkaew S, Gutkind JS. A role for p38 MAPK in head and neck cancer cell growth and tumor-induced angiogenesis and lymphangiogenesis. Mol Oncol. 2014;8(1):105–18.
18. Reustle A, Torzewski M. Role of p38 MAPK in atherosclerosis and aortic valve sclerosis. Int J Mol Sci. 2018;19(12):3761.
19. Miura H, Kondo Y, Matsuda M, Aoki K. Cell-to-cell heterogeneity in p38-mediated cross-inhibition of JNK causes stochastic cell death. Cell Rep. 2018;24(10):2658–68.
20. Lin CL, Lee CH, Chen CM, Cheng CW, Chen PN, Ying TH, et al. Protodioscin induces apoptosis through ROS-mediated endoplasmic reticulum stress via the JNK/p38 activation pathways in human cervical cancer cells. Cell Physiol Biochem. 2018;46(1):322–34.
21. Lawrence T. The nuclear factor NF-kappaB pathway in inflammation. Cold Spring Harb Perspect Biol. 2009;1(6):a001651.
22. Grynberg K, Ma FY, Nikolic-Paterson DJ. The JNK signaling pathway in renal Fibrosis. Front Physiol. 2017;8:829.
23. Tredwell M, Preshlock SM, Taylor NJ, Gruber S, Huiban M, Passchier J, et al. A general copper-mediated nucleophilic ^{18}F fluorination of arenes. Angew Chem Int Ed Engl. 2014;53(30):7751–5.
24. Lim SSD, Jeon S, Kim Y, Kim H, Lee S, Cho H, Lee BC, Kim SE, Kim K, Lee E. Cobalt-catalyzed C-F bond borylation of aryl fluorides. Org Lett. 2018;20(22):7249–52.
25. Niwa TOH, Watanabe Y, Hosoya T. Ni/Cu-catalyzed defluoroborylation of fluoroarenes for diverse C-F Bond functionalizations. J Am Chem Soc. 2015;137(45):14313–8.
26. Airaksinen AJ. The radiopharmaceutical chemistry of Fluorine-18: next-generation fluorinations. Radiopharmaceutical Chemistry. 2019:297–310.
27. Makaravage KJBA, Mossine AV, Sanford MS, Scott PJH. Copper-mediated radiofluorination of arylstannanes with [^{18}F]KF. Org Lett. 2016;18(20):5440–3.